

Article

Corrosion Behaviors of Outdoor Bronze Sculptures in an Urban–Industrial Environment: Corrosion Experiment on Artificial Sulfide Patina

Heehong Kwon ¹  and Namchul Cho ^{2,*}

¹ Department of Conservation and Art Bank, National Museum of Modern and Contemporary Art, Cheongju 28501, Republic of Korea; entasis@korea.kr

² Department of Cultural Heritage Conservation Science, Kongju National University, Gongju 32588, Republic of Korea

* Correspondence: nam1611@kongju.ac.kr; Tel.: +82-41-850-8570

Abstract: Copper alloys interact with air pollutants to form corrosion products and, consequently, a patina on outdoor bronze sculptures. In this study, corrosion experiments were conducted to clarify the corrosion behaviors of artificial sulfide patina in an urban–industrial environment on a quaternary bronze alloy (Cu–Zn–Sn–Pb) with a composition and metallurgical properties similar to those of outdoor bronze sculptures. The correlation between the chromaticity and reflectance of the patina revealed increasing brochantite with the corrosion of the patina and an association between the chromaticity a^* and patina growth. Cuprite and brochantite were distinguished, and the point at which brochantite covered the patina surface was determined. The quantitative changes in brochantite were mainly influenced by physical causes such as the crystal size and patina layer thickness as well as by Cu^{2+} ions working as color formation ions moving to the outermost layer. Atmospheric corrosion of the alloy resulted in reduced Cu and Zn contents and increased Sn and Pb contents. The patina consisted of brochantite in the outermost layer and cuprite and cassiterite in the inner layers. These findings should clarify corrosion characteristics such as the surface color, composition, and changes in corrosion products of outdoor bronze sculptures and contribute toward their preservation.



Citation: Kwon, H.; Cho, N. Corrosion Behaviors of Outdoor Bronze Sculptures in an Urban–Industrial Environment: Corrosion Experiment on Artificial Sulfide Patina. *Metals* **2023**, *13*, 1101. <https://doi.org/10.3390/met13061101>

Academic Editor: Elena Gordo

Received: 18 May 2023

Revised: 6 June 2023

Accepted: 7 June 2023

Published: 11 June 2023



Copyright: © 2023 by the authors. Licensee MDPI, Basel, Switzerland. This article is an open access article distributed under the terms and conditions of the Creative Commons Attribution (CC BY) license (<https://creativecommons.org/licenses/by/4.0/>).

Keywords: outdoor corrosion; patina; brochantite; cuprite; bronze sculpture

1. Introduction

Copper alloys are frequently used in outdoor sculptures. However, they gradually corrode with prolonged exposure to outdoor environments owing to temperature and humidity changes, air pollution, ultraviolet rays, and biological damage [1]. In particular, corrosion products are formed in outdoor bronze sculptures through interactions between copper alloys and air pollutants, resulting in the formation of a patina of various types of corrosion products. Acid rain containing SO_2 , NO_2 , and O_3 , which are typically found in an urban–industrial environment, and chloride in a marine environment causes color changes and damages the protective patina that adds esthetic and historical value to sculptures.

The patina on outdoor bronze sculptures exhibits various colors (e.g., black, red, and green), stains, and cracks (Figure 1). A bronze surface initially becomes brownish or black and eventually exhibits an esthetically pleasing green patina. The appearance of the patina is mainly determined by the luster, color, and surface condition of the metal surface. For example, the color of copper alloys is known to be affected by their composition. Therefore, the characteristics of the copper alloys and patina must be first identified to distinguish the types of corrosion products. Similarly, bronze sculptures exhibit a unique color depending on their composition, and their corrosion products have specific colors [2]. The composition, structure, and color of bronze must be analyzed to understand the

corrosion process occurring on its surface. If corrosion products formed on a bronze surface are identified and characterized based on such information, the corrosion types and causes can be identified.



Figure 1. Outdoor bronze sculptures in urban–industrial environments (collections of the National Museum of Modern and Contemporary Art, Republic of Korea).

Studies have investigated the corrosion mechanism of binary (Cu–Sn) and ternary (Cu–Sn–Pb) copper alloy systems. Further, around 500 bronze sculptures made in Republic of Korea or other countries since the 20th century were made of a quaternary alloy (Cu–Zn–Sn–Pb) [3–9]. Such sculptures were produced using valves, cartridge cases, or scrap metal generated when dismantling ships, with Zn serving to distinguish the casting methods and foundry characteristics and to classify the composition ratios according to the use of sand mold or wax casting methods [5,8].

In this study, corrosion experiments were conducted on the artificial patina of a quaternary bronze alloy (Cu–Zn–Sn–Pb) with a composition and metallurgical properties similar to those of outdoor bronze sculptures to investigate the corrosion behaviors of sulfide patinas that are commonly found in urban–industrial environments. Specifically, the surface color, composition, and changes in the corrosion products of the patina with its growth were examined.

2. Methods

2.1. Corrosion Experiment on Artificial Patina

Bronze specimens were produced with the constituent alloys of an outdoor bronze sculpture and an experimental specimen from a previous study (dimensions: 30 mm × 50 mm × 3 mm, 5 mm × 5 mm × 3 mm) for use in corrosion experiments on an artificial patina; Table 1 lists their compositions. Specimens were perforated at the top so that they could be easily dipped in a corrosive solution. Because the surface texture affects the reflection of light, the specimens were uniformly abraded with #1000 sandpaper [10,11]. Then, they were dipped in ethanol to remove any remaining foreign substances and cleaned using an ultrasonic cleaner.

To reproduce corrosion products caused by sulfide, a major air pollutant in urban–industrial environments, an aqueous solution of 50 mM copper sulfate (CuSO₄) (in deionized water) was prepared as a corrosive solution based on previous studies [12–16]. In the corrosion experiment, the specimen was deposited in this corrosive solution for 24 h,

removed from the solution, and naturally dried for 24 h at 20–24 °C and RH 45–55%. This cycle was repeated 50 times to gradually form an artificial sulfide patina (Table 2).

Table 1. Composition of bronze specimen for corrosion experiment of artificial patina.

Composition (wt%)				
Cu	Zn	Sn	Pb	Total
88.8	5.1	3.1	3	100

Table 2. Corrosive solution for producing artificial sulfide patina.

Category	Patina	Sulfide Patina
	Corrosive solution Specimen fabrication	Aqueous solution of 50 mM CuSO ₄ (in deionized water) 50 cycles of (24 h deposition → 24 h natural drying)

2.2. Analyses

2.2.1. Analysis of Surface Condition and Form

To analyze the surface condition and form of the artificial patina, the specimen was photographed using a digital camera (EOS 6D Mark II, Canon, Japan) and observed using a microscope (RH-2000, Hirox, Japan).

2.2.2. Analysis of Chromaticity and Reflectance

To analyze the color of the artificial patina, the chromaticity and reflectance were numerically measured. Measurements were performed using a spectrum colorimeter (CR-400, Minolta, Japan) in the specular component excluded (SCE) mode with a measurement diameter of $\varnothing 3$ mm. The surface reflectance was calculated as an average of five measurements in the visible light range (350–750 nm).

2.2.3. Analysis of Corrosion Products

X-ray diffraction (XRD) analysis (D8 Advance with DAVINCI, Bruker, Germany) was performed to accurately analyze the crystal structure of corrosion products formed on the artificial patina surface. A copper (Cu $\kappa\alpha_1$ 1.5418 Å) target was used with a current and accelerating voltage of 40 mA and 40 kV, respectively, in the X-ray tube. The analysis was performed with a diffraction angle of 2θ of 10–90°, step size of 0.02°, and scan speed of 0.5 s/step. The XRD patterns were analyzed using the Crystallography Open Database (COD) and TOPAS software; further, they were quantitatively analyzed according to industrial needs for the Rietveld method by using Siroquant v. 3.0 [17].

Raman spectroscopy (LabRam ARAMIS, Horiba Jobin-Yvon, France) using a 514 nm Nd:YAG laser and a grating of 600 gr/mm and resolution of ~ 3.0 cm⁻¹ was used to analyze the corrosion products of each artificial patina layer. The analysis equipment had a scan range of 150–4200 cm⁻¹; however, only data in the range of 100–1500 cm⁻¹ were analyzed to match where the characteristics of corrosion products were exhibited. The acquired Raman spectrum was comparatively analyzed against the results of previous studies as well as references provided by the Infrared & Raman Users Group (IRUG), Synthetic Organic Pigments Research Aggregation Network (SOPRANO), and RRUFF Project.

2.2.4. Analysis of Microstructure and Composition

The specimen was mounted on epoxy resin to examine the surface and cross section of the artificial patina layer by scanning electron microscopy with energy-dispersive spectroscopy (SEM-EDS; JSM-6610LV, Jeol, JP/X-Max, Oxford, UK) in the secondary electron image (SEI) mode at 15 kV with a spot size of 55 and WD of 10 mm. The specimen was sequentially abraded using sandpaper (#220–4000); then, scratches on its surface were ultimately removed through fine abrasion (3 μ m, 1 μ m). Finally, the microstructure of the

specimen was observed using a microscope (KH-7700, Hirox, Japan). The thickness of the cross section of the patina was indicated by the measured maximum and minimum values.

3. Results

3.1. Microstructure and Material Characteristics of Specimen

Before conducting the corrosion experiment on the artificial patina, observations of the surface and microstructure of the specimen (Figure 2) revealed a dendritic α phase, which is commonly observed in Cu–Zn–Sn–Pb alloy sculptures [15,18–21] with relatively low Sn content. The observed microstructure was mostly similar to a cast structure to which artificial processing such as heat treatment has not been applied [22].

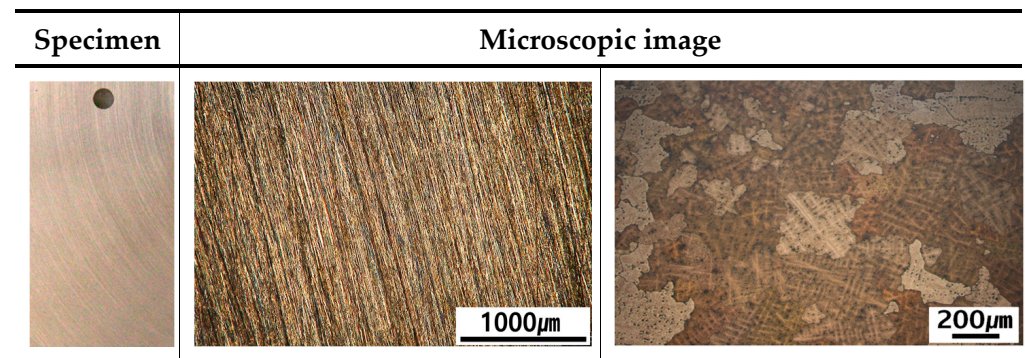


Figure 2. Surface and microstructure of specimen before artificial patina corrosion experiment.

3.2. Surface Form and Condition

To reproduce corrosion products generated in an urban–industrial environment, experiments were performed on the bronze specimen for 2400 h (i.e., 50 times) by using an aqueous solution of 50 mM CuSO_4 , as shown in Figure 3. The specimen color changed to reddish only 48 h (S1) after the corrosion experiment started, and it subsequently changed to reddish brown (~S5) and dark brown (~S8). In particular, starting from the center of the specimen, the color started to change from reddish brown to a yellow patina after 240 h (S5). This was also observed in microscopic images, where a patina in the form of a green dot was first observed after 144 h (S3), and the specimen surface began to be covered by a green patina after 240 h (S5).

The green region gradually became larger, and a thick and dark green patina covered almost the entire surface after 432 h (S9). The color of the patina quickly changed up until this point, following which it gradually changed after 576 h (S12). After 1920 h (S30), a dark-green patina completely covering the reddish-brown patina was obtained. Until the end of the experiment at 2400 h (S50), the green patina gradually became denser.

3.3. Chromaticity and Reflectance

To quantitatively measure the color of the artificial patina, chromaticity analysis values were obtained in the CIE $L^*a^*b^*$ space (Figure 4), where L^* was 53.5–58.86, and its maximum deviation was 5.36. With time, the lightness (L^*) value gradually increased, thus brightening the color. The a^* value indicates green and red colors; it ranged between -10.06 and 10.95 , and its maximum deviation was 21.01. The a^* value gradually decreased as corrosion progressed, thus becoming closer to a green color. Previous surface form analysis results indicated that the color changed quickly up until 240 h (S5), and subsequent changes followed those in the a^* value. The b^* value indicates blue and yellow colors; it ranged between 1.08 and 11.15, and its maximum deviation was 10.07. The b^* value gradually decreased as corrosion progressed, thus becoming closer to a blue color. In other words, L^* and a^* were correlated with the growth of the green patina in the group exposed to sulfide as an air pollutant.

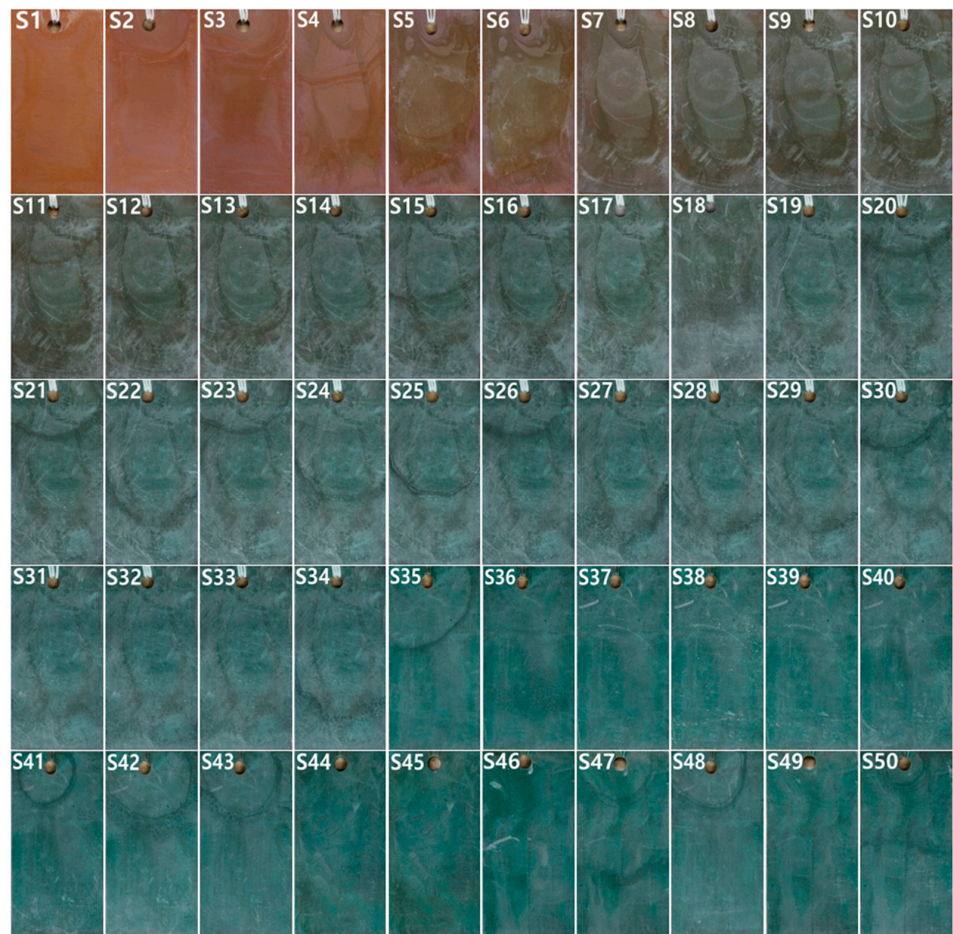


Figure 3. Corrosion experiment of artificial sulfide patina: specimen image.

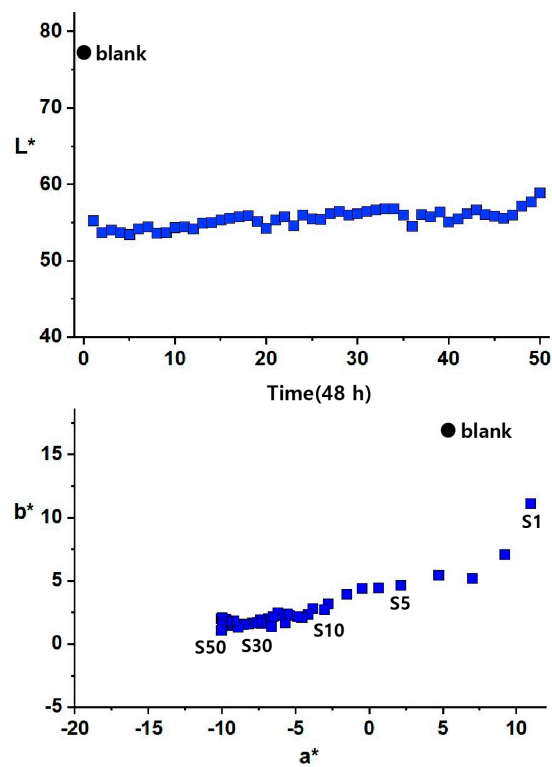


Figure 4. Chromaticity analysis graph of artificial sulfide patina.

The color of the artificial patina is affected by the reflectance, which has a complementary color correlation. In a complementary color correlation, blue is affected by the reflectance of yellow, and red is affected by the reflectance of green. In this light, the reflectance of the artificial patina was analyzed using the difference in the reflectance between color wavelengths. The reflectance was distinguished according to the wavelengths of each color: blue (380–500 nm), green (500–565 nm), yellow (565–625 nm), and red (625–750 nm). Figure 5 shows the measurement results of the reflectance of the artificial sulfide patina in visible light.

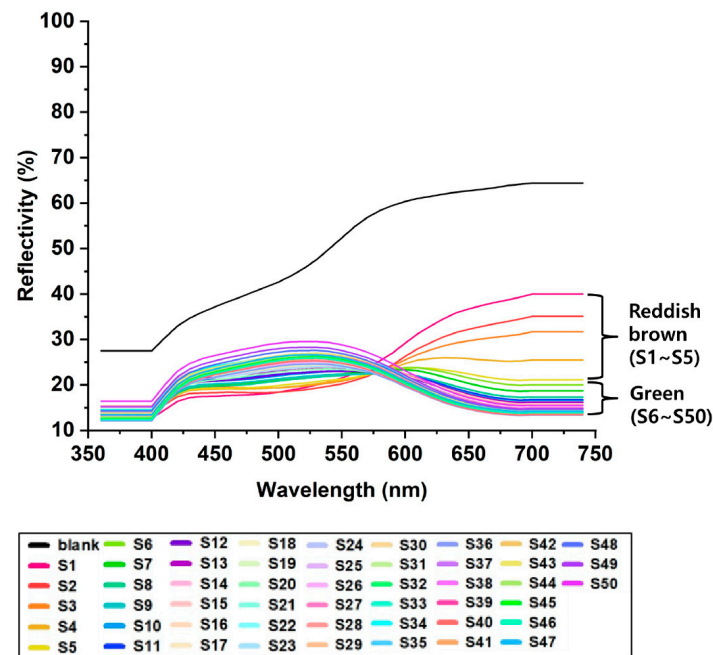


Figure 5. Reflectance analysis graph of artificial sulfide patina.

The reflectance spectrum analysis results indicated that a red patina (S1–S5) and green patina (S6–S50) were clearly distinguished in the corrosion experiment on the artificial sulfide patina. The red patina exhibited low reflectance in blue and green colors but high reflectance in yellow (565–625 nm) and red (625–750 nm) colors. In particular, the reflectance of red drastically decreased with corrosion (S1–S5); this corresponds to the chromaticity analysis results. The above results imply that a red patina quickly decreases.

The green patina gradually exhibited a higher reflectance in blue (380–500 nm) and green (500–565 nm) colors, in line with the chromaticity analysis results, and it exhibited the highest reflectance after 2400 h (S50); however, it exhibited lower reflectance in yellow and red colors. Thus, a green patina should continue to grow with corrosion.

3.4. Analysis of Corrosion Products

XRD analysis was performed to identify and semiquantitatively analyze the corrosion products of the artificial patina surface. From S1, when the color began to change, to S50, when the experiment ended, eight cycles were semiquantitatively analyzed to examine the trend of quantitative changes in the corrosion products (Figure 6). The XRD analysis results confirmed cuprite (Cu_2O) and brochantite ($\text{Cu}_4\text{SO}_4(\text{OH})_6$) as two major corrosion products, along with zincite (ZnO), zinkosite (ZnSO_4), copper zinc (Cu_3Zn), copper tin ($(\text{Cu}_{32}\text{Sn})_{0.12}$), and lead oxide.

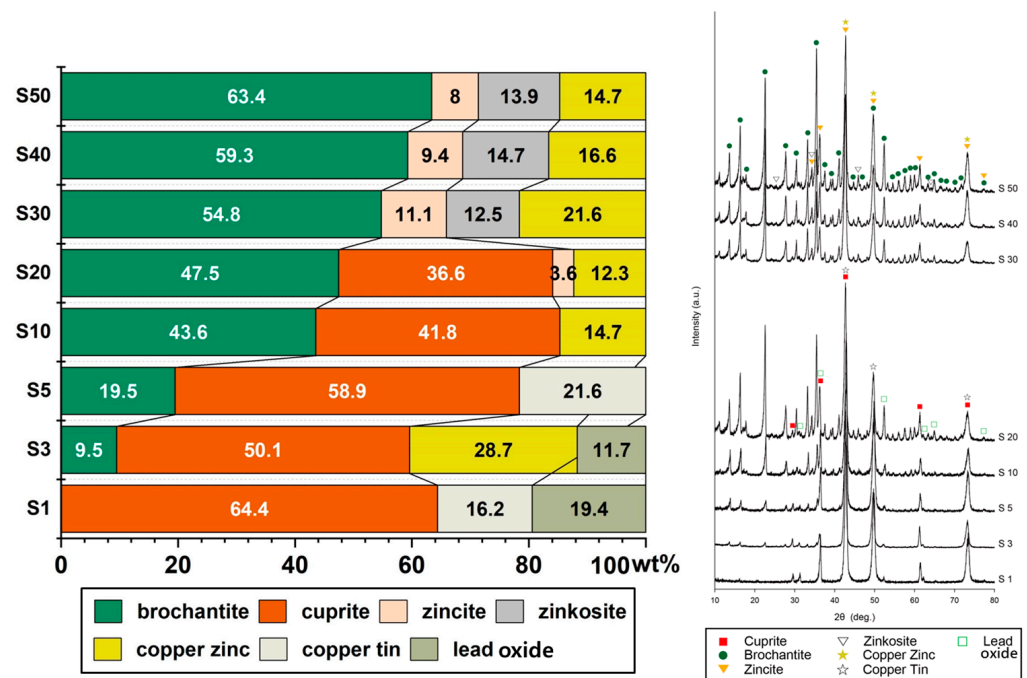


Figure 6. XRD semiquantitative analysis graph of artificial sulfide patina surface.

At S1 (48 h), 64.4% cuprite was detected when the specimen color started to change to red at the beginning of the corrosion experiment, and the value decreased by 14.3% to 50.1% at S3 (144 h) when a green spot started to appear. At S5 (240 h), 58.9% cuprite was detected when the specimen started to be covered by the green patina, and the value decreased to 41.8% at S10 (480 h) and 36.6% at S20 (960 h) when the color started to change to green. After S30 (1440 h), cuprite was not detected on the specimen surface. This was judged to be the time when green brochantite completely covered the party or surface.

In contrast, brochantite was not detected at S1 (144 h) when the color initially changed to red; however, 9.5% brochantite was first detected at S3 (144 h) when a green spot started to appear. Further, 19.5% brochantite was detected at S5 (240 h) when the specimen started to be covered by a green patina, and the value increased to 43.6% at S10 (480 h) and 47.5% at S20 (960 h) when the color started to change to green. Finally, 54.8% brochantite was detected at S30 (1440 h) when the specimen was completely covered by a green patina, and 63.4% brochantite was detected at S50 (2400 h) as the patina continued to grow when the corrosion experiment ended.

In general, two layers of patina (i.e., cuprite, brochantite) form on bronze exposed to air. Cuprite increases up to a certain point and then the corrosion rate starts to decrease, whereas brochantite increases constantly, in keeping with the corrosion characteristics of outdoor bronze sculptures [13,16,23–25]. Furthermore, Cu–Sn ((Cu₃₂Sn)_{0.12}) and lead oxide were observed at the beginning of the experiment owing to Sn oxide and Pb segregates resulting from corrosion. After S10, zinc oxides such as zincite, zinkosite, and copper zinc were observed.

3.5. Microstructure and Composition of Corrosion Products

The composition and corrosion products of each layer were examined through SEM-EDS and Raman analyses (Figure 7, Table 3). Subsequently, EDS area analysis was performed to study the changes in the constituent alloys with corrosion. In addition, the crystal structure and cross section in each cycle of the corrosion experiment on the artificial sulfide patina were observed through visual inspection, optical microscopy, and SEM, as shown in Figure 8, and enlarged images of cuprite and brochantite crystals are shown in Figures 9 and 10, respectively.

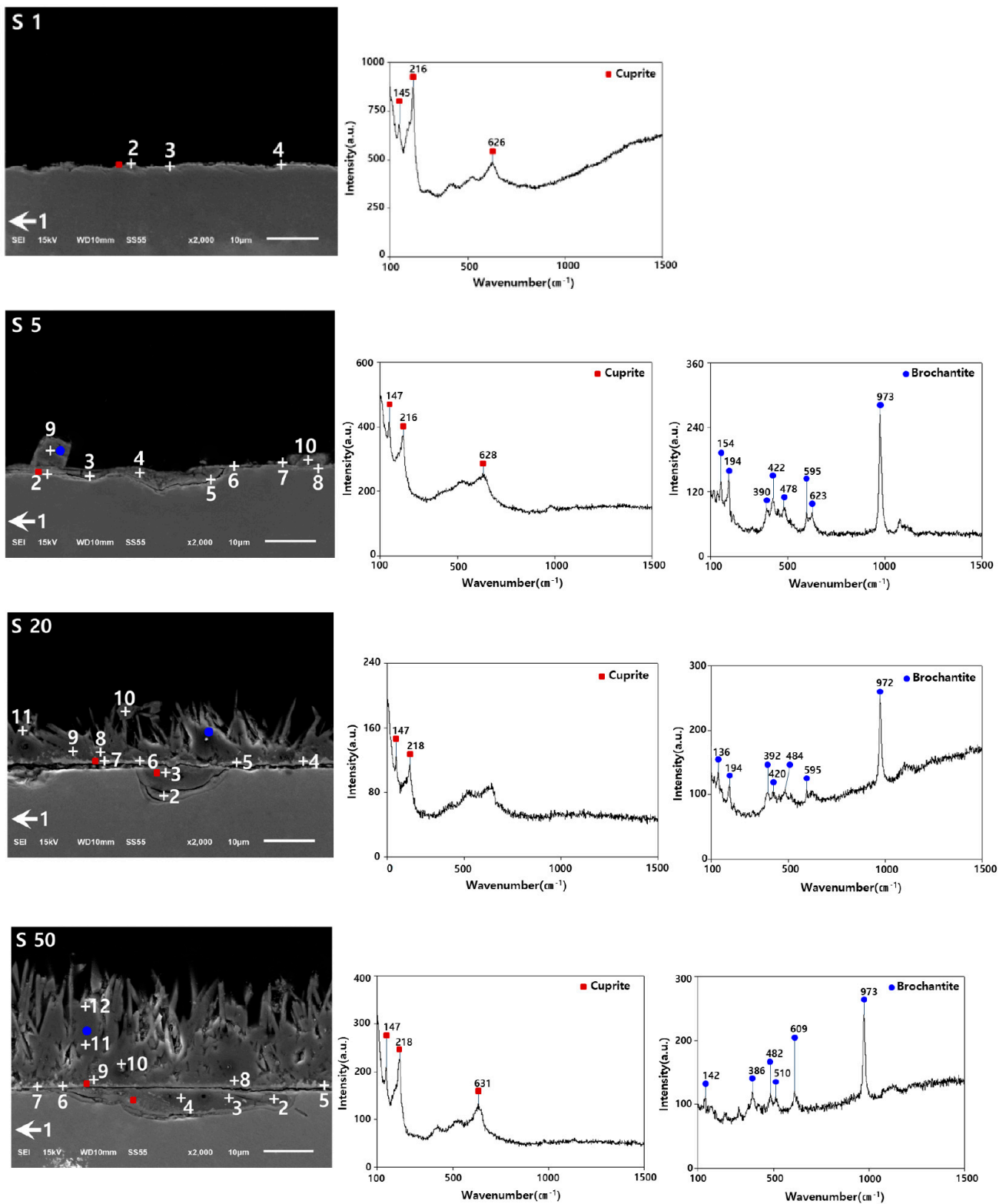


Figure 7. SEM-EDS, Raman analysis location, and Raman analysis graph for artificial sulfide patina.

Table 3. SEM-EDS analysis result of artificial sulfide patina.

No.	Position	Composition (wt%)						Layer
		Cu	Zn	Sn	Pb	O	S	
S1	1	88.80	7.97	2.93	0.12	-	-	bronze
	2	80.11	1.90	1.46	0.90	15.40	0.23	cuprite
	3	79.01	1.11	1.69	0.69	16.87	0.63	
	4	77.76	0.94	1.2	0.51	19.57	-	
S5	1	88.58	7.90	3.00	0.12	0.40	-	bronze
	2	63.94	1.83	12.26	0.80	20.30	0.87	cuprite, cassiterite
	3	64.93	1.04	12.07	0.97	19.98	1.00	
	4	69.75	2.96	8.54	0.97	17.06	0.71	
	5	61.01	0.97	12.90	0.95	23.54	0.63	
	6	78.98	1.94	2.69	0.32	15.73	0.35	cuprite
	7	81.58	1.48	1.17	0.54	14.67	0.56	
	8	84.23	1.39	0.98	0.52	12.87	-	
	9	61.96	0.27	0.88	0.71	30.08	6.09	brochantite
	10	60.49	0.64	0.74	0.21	31.85	6.08	
S20	1	87.72	7.40	4.57	-	0.31	-	bronze
	2	61.71	0.10	13.51	1.47	22.46	0.75	cuprite, cassiterite
	3	59.53	0.45	9.07	1.39	25.76	3.80	
	4	83.59	0.87	0.68	0.83	14.02	0.01	cuprite
	5	84.21	0.92	0.96	0.65	13.26	-	
	6	85.27	0.91	1.17	0.15	12.51	-	
	7	81.13	1.39	0.67	0.47	15.92	0.43	
	8	60.96	-	0.39	1.31	28.67	8.68	brochantite
	9	61.57	0.12	0.65	1.26	28.75	7.64	
	10	62.10	0.13	0.51	1.79	27.23	8.24	
	11	64.62	0.03	0.56	1.15	26.27	7.37	
12	64.62	0.03	0.56	1.15	26.27	7.37		
S50	1	82.10	6.80	4.14	6.11	0.84	-	bronze
	2	36.05	0.58	29.42	1.95	29.60	2.39	cassiterite
	3	47.90	-	13.35	2.05	27.91	8.79	
	4	55.71	0.04	6.07	1.37	27.59	9.23	cuprite, cassiterite
	5	84.38	0.39	0.33	0.51	14.37	0.03	cuprite
	6	83.64	0.66	0.92	0.37	14.41	0.01	
	7	79.33	0.69	0.52	0.82	17.20	1.44	
	8	66.52	0.47	0.62	1.07	23.98	7.34	brochantite
	9	68.93	0.46	0.51	0.91	22.96	6.22	
	10	68.58	-	0.35	1.18	23.56	6.33	
	11	66.03	-	0.24	0.79	25.13	7.80	
	12	67.31	-	0.14	1.08	25.62	5.85	

At S1 (48 h), when the specimen color changed to reddish at the beginning of the experiment, an octahedral cubic crystal structure of 1–2 μm was formed through repeated condensation on top of the base layer. Observations of the cross section revealed a 0.1–0.3 μm thick layer with porous voids, and EDS analysis revealed high Cu (about 77–80 wt%) and O (about 15–19 wt%) contents. These results correspond to the cuprite crystal confirmed by the Raman analysis results. The EDS area analysis revealed a composition of 88.80 wt% Cu, 7.97 wt% Zn, 2.93 wt% Sn, and 0.12 wt% Pb (S1 in Figure 7 and Table 3: 1–4).

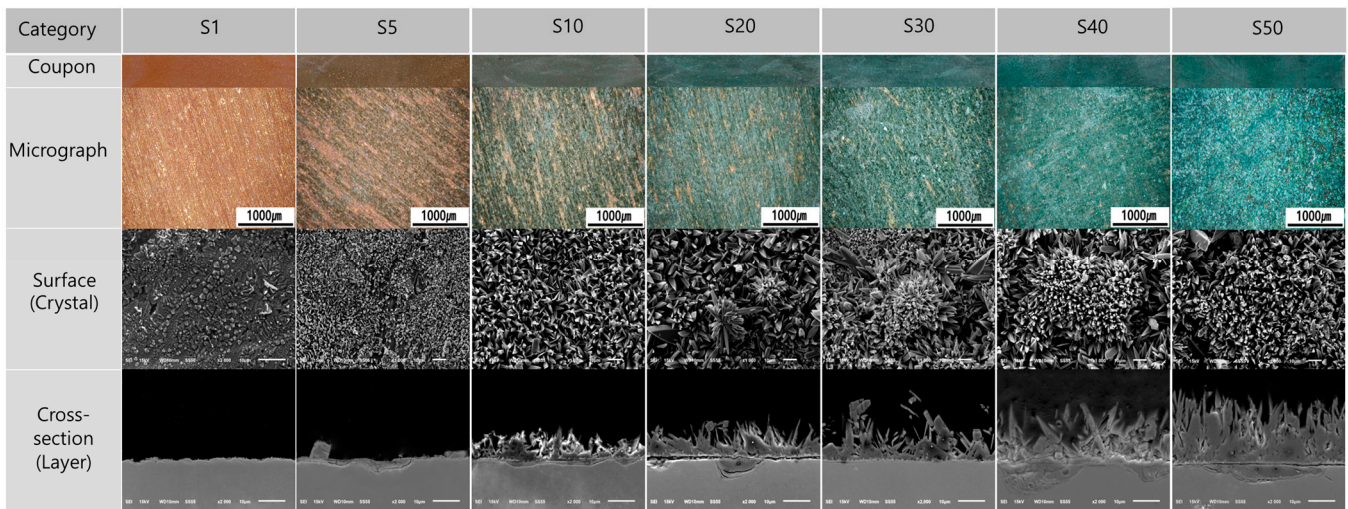


Figure 8. Growth stages of sulfide patina: optical, microscopy, and SEM images.

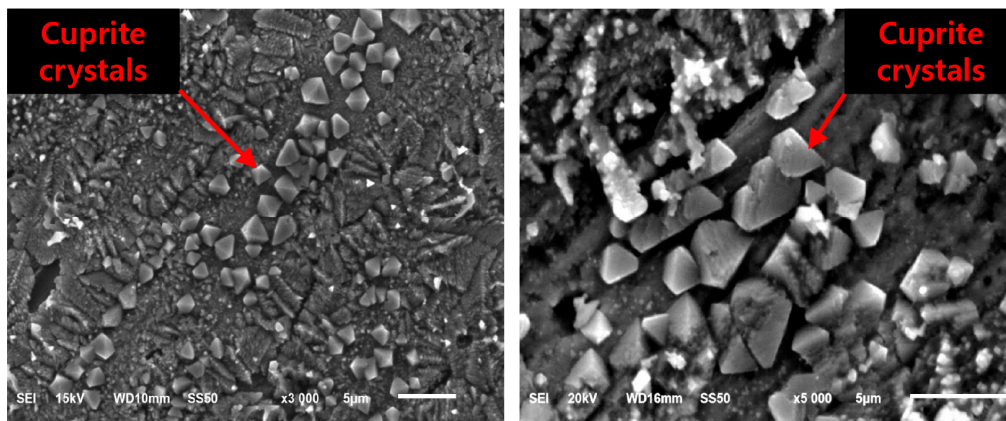


Figure 9. SEM image of cuprite crystal.

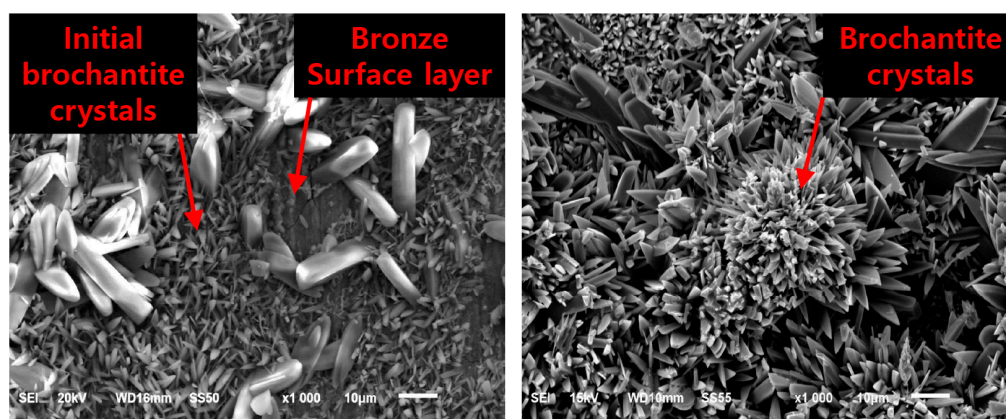


Figure 10. SEM image of (left) initial and (right) mature brochantite crystal.

At S5 (240 h), a needle-like monoclinic crystal (length: 2–8 μm , width: 1–3 μm) was densely formed on top of the base layer. Observations of the cross section revealed a 0.1–3 μm thick layer on top of a void at the boundary with the base layer, and a monoclinic crystal with a height of 2–5 μm on top.

The SEM-EDS analysis revealed a higher ratio of Cu (about 61–84 wt%) and O (about 12–23 wt%) in the internal layer (S5 in Figure 7 and Table 3: 2–8). However, the Sn

composition differed by 8.54–12.90 wt% at analysis locations 2–5 and 0.98–2.69 wt% at analysis locations 6–8, representing a significant variation. The EDS area analysis revealed a composition of 88.58 wt% Cu, 7.90 wt% Zn, 3.00 wt% Sn, and 0.40 wt% Pb.

Previous analyses of Cu–Zn–Sn–Pb and Cu–Sn–Zn bronze under atmospheric environmental conditions revealed a mixture of cuprite and cassiterite (SnO₂) in a reddish-brown patina formed on the base metal [26–29]. However, it is difficult to accurately distinguish cuprite and cassiterite through XRD and Raman analysis [30–32]. Cassiterite is known to be amorphous or nanocrystalline, and, therefore, the possibility of detecting it is low because the characteristic peak detected at 633 cm^{−1} is significantly close to the wide and strong characteristic peak of cuprite near 625 cm^{−1}. Therefore, when cassiterite and cuprite coexist, the former is difficult to detect [31]. In this study, only cuprite was analyzed in the Raman analysis; at S5 (240 h), cuprite and cassiterite were highly likely to be mixed in the layer with high Sn content. Needle-like crystals in the outer layer had a high ratio of Cu (about 60–61 wt%), S (about 6 wt%), and O (about 30–31 wt%); they were confirmed as brochantite, as also confirmed in the Raman analysis.

At S20 (960 h), a flower-shaped crystal with a diameter of 10–20 μm was observed between densely formed, needle-like crystals. Observations of the cross section revealed semicircular (7 μm) pitting between the base layer; Raman analysis of this pitting confirmed the presence of cuprite. However, EDS analysis revealed a high ratio of Cu (about 59–61 wt%), O (about 22–25 wt%), and Sn (about 9–13 wt%), indicating that cuprite and cassiterite were most likely mixed (S20 in Figure 7 and Table 3: 2, 3). A 0.3–0.5 μm thick internal layer was formed on top of a void at the boundary with the base layer; it was analyzed to have a high ratio of Cu (about 81–85 wt%) and O (about 12–15 wt%), confirming that it was cuprite, as in the Raman analysis (S20 in Figure 7 and Table 3: 4–7). Needle-like monoclinic crystals with a length of 3–12 μm formed an outer layer on the top; they were analyzed to have a higher ratio of Cu (about 60–64 wt%), S (about 7–8 wt%), and O (about 26–28 wt%), confirming that they were brochantite, as in the Raman analysis. EDS area analysis revealed a composition of 87.72 wt% Cu, 7.40 wt% Zn, and 4.57 wt% Sn.

At S50 (2400 h), needle-like crystals formed a flower-shaped crystal aggregate with a diameter of 50 μm. Observations of the cross section revealed pitting with a thickness of 1–6 μm between the base layer; on the top of the pitting, an internal layer of 0.3–0.5 μm thickness and 12–20 μm needle-like monoclinic crystals formed the outer layer. Raman analysis of the pitting and internal layer confirmed the presence of cuprite, and SEM-EDS analysis showed that the Sn composition at S50 was 13.35–29.42 wt% at locations 2–3, 6.07 wt% at location 4, and 0.33–0.92 wt% at locations 5–7, most likely corresponding to a cassiterite layer, a cuprite and cassiterite mixed layer, and a cuprite layer, respectively (Figure 7, Table 3). The needle-like crystals in the outer layer had a high ratio of Cu (about 66–68 wt%), S (about 6–7 wt%), and O (about 22–25 wt%), and they were confirmed as brochantite with a composition of 82.10 wt% Cu, 6.80 wt% Zn, 4.14 wt% Sn, and 6.11 wt% Pb.

4. Discussion

This study examined the corrosion characteristics and changes in the chemical composition of outdoor bronze sculptures through a corrosion experiment on artificial sulfide patina found in an urban–industrial environment and examined the formation process of sulfide patina. In particular, by conducting corrosion experiments on artificial patina, standard data relating to individual corrosion products such as copper oxide (cuprite) and sulfide patina (brochantite), which are typically observed during the corrosion of outdoor bronze sculptures, were obtained. However, multiple corrosion products are detected in actual outdoor environments [33–36]; occasionally, other pollutants such as soil minerals, soot, and ashes may also be detected.

4.1. Correlation between Color Classification and Corrosion Products of Sulfide Patina

When the correlation between the quantitative changes in corrosion products and the surface color changes of the artificial sulfide patina was analyzed in terms of corrosion behaviors, the patina colors were largely classified into two types based on the color difference (ΔE^*) and reflectance (Figures 4, 5 and 8). The color difference of S1–S5 was around 21 (32→11), and it decreased considerably in a short period of time (240 h), whereas that of S6–S50 was around 4 (5→0.9), and it remained constant over a long period of time (2152 h). This result was more noticeable with the chromaticity a^* , which represents blue and green colors. The chromaticity a^* value of S1–S5 decreased significantly by 8 over a short period of time, whereas that of S6–S50 gradually changed by 10 over a long period of time. The reflectance also increased consistently in the blue–green wavelength (380–565 nm) and then an inflection point appeared at around 570 nm. The reflectance of S1–S5 decreased substantially by 20 in the yellow–red wavelength (565–750 nm), and that of S6–S50 decreased by less than 8. At S5, the specimen was seen to be covered by a green patina visually and through a microscope; XRD analysis also revealed brochantite, a basic copper sulfide (19.5%). Therefore, the artificial sulfide patina was classified into two colors, in line with the characteristics of the patina that is commonly generated in an urban–industrial environment.

A comparison of the chromaticity values and quantitative changes in the corrosion products of the artificial sulfide patina revealed that cuprite decreased continuously after initial generation, and the chromaticity value decreased proportionally, whereas green brochantite increased gradually, and the chromaticity value changed in an inversely proportional manner (Figure 11).

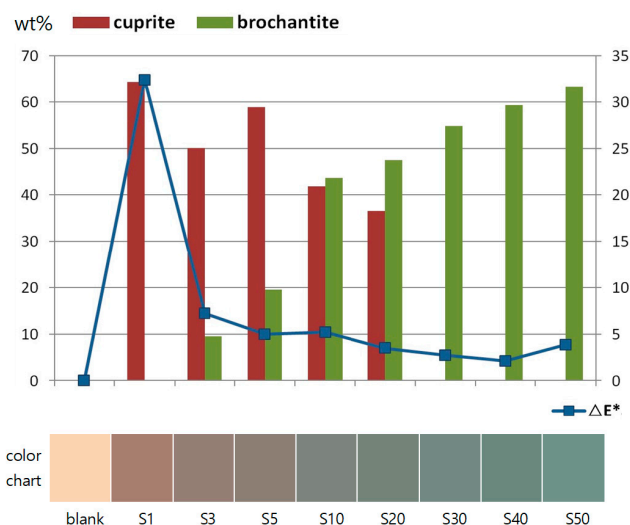


Figure 11. Chromaticity comparison graph of corrosion products of artificial sulfide patina.

This tendency can be explained by the difference between the optical characteristics of cuprite and brochantite. The optical characteristics of reddish-brown cuprite are not greatly affected by the environment; however, the semiconductor characteristics and an impurity such as hydrogen (H) in the aqueous film on the bronze surface moving into cuprite affect the defect structure. Brochantite appears green because Cu^{2+} acts as a color-forming ion; the layer needs to be at least $12 \pm 2 \mu\text{m}$ thick to form a blue-green patina [37]. In this study, the specimen was completely covered by a green patina, and cuprite was not detected on the specimen surface after S30 (1440 h); at this time, the brochantite layer had a thickness of $15 \mu\text{m}$ or higher.

4.2. Correlation between Composition and Corrosion Products of Sulfide Patina

An analysis of the correlation between the composition and the corrosion products of the artificial sulfide patina in terms of the corrosion behavior (Figure 12) revealed

that reddish-brown cuprite was formed early in the corrosion experiment; however, its amount decreased over time. Further, the amount of green brochantite, a basic copper sulfate, gradually increased to 63.4% until the end of the experiment. The changes in the composition of the bronze base layer revealed that the Cu and Zn contents decreased, whereas the Sn and Pb contents relatively increased. These results are in line with the corrosion mechanisms of Cu–Zn–Sn–Pb and Cu–Zn–Sn alloys and the findings of previous studies [20,30,31,37–39].

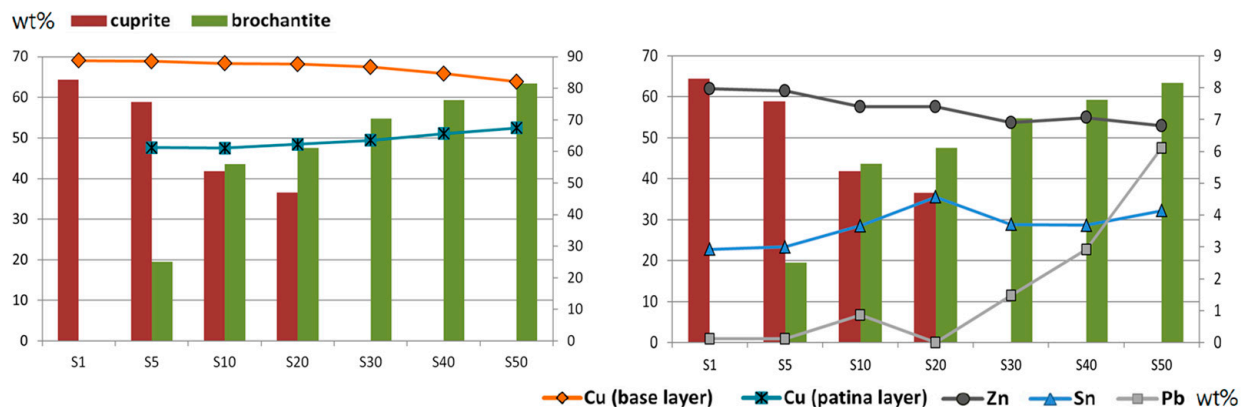


Figure 12. Correlation graph of composition and corrosion products of artificial sulfide patina with respect to corrosion behavior.

The decrease in Cu and Zn is respectively attributable to the selective dissolution of Cu and Zn ions owing to the decuprification and dezincification processes within bronze; the cation moves toward the boundary through the patina inside the alloy, and the anion moves toward the inside of the alloy [37,39,40]. In particular, the initial corrosion is mainly (>90%) caused by Cu and Zn [31,38]; Sn forms a patina layer upon condensing as it is an insoluble corrosion product and is known to stabilize the patina through passivation [30,41].

The EDS area analysis of the base metal showed that the Cu content decreased by 6.7 wt% (88.8 (S1) → 88.58 (S5) → 87.92 (S10) → 87.74 (S20) → 86.8 (S30) → 84.72 (S40) → 82.1 (S50)), and the average value of Cu in the outermost corrosion layer increased by 6.37 wt% (61.2 (S5) → 61.08 (S10) → 62.31 (S20) → 63.62 (S30) → 65.75 (S40) → 67.47 (S50)). It can, therefore, be inferred that the major factors determining the quantitative changes in brochantite may include physical causes such as crystal size and patina layer thickness; another factor is the increase in Cu that occurs when Cu^{2+} ions working as color formation ions move to the outermost layer. Therefore, the increase in the Cu content in the sulfide patina is correlated with the green patina (i.e., growth of brochantite).

4.3. Corrosion Mechanism of Sulfide Patina

Figures 13 and 14 illustrate the formation process of the sulfide patina and atmospheric corrosion mechanism, respectively. The sulfide patina formed three layers consisting of an outer brochantite layer and inner cuprite and cassiterite layers. In the early stages of the corrosion experiment, 1–3 μm octahedral cubic crystals formed a thin cuprite layer with a thickness of 0.1–0.3 μm on top of the base bronze layer. The cuprite thickness was consistently maintained at 0.1–0.5 μm until the end of the experiment.

Then, cassiterite was formed around the pitting between the base metal and cuprite. Several studies conducted under outdoor environmental conditions revealed that cuprite and cassiterite are mixed in the reddish-brown patina formed on top of the base metal. At S50 (2400 h), the artificial patina comprised cuprite (Cu: 79.33–84.38 wt%, Sn: 0.33–0.92 wt%), cassiterite (Cu: 55.71 wt%, Sn: 6.07 wt%), and a mixed layer of cassiterite and cuprite (Cu: 36.05–47.90 wt%, Sn: 13.35–29.42 wt%), based on the Cu and Sn contents and structure of each layer.

surface is restrained, and light-green or striped spots can be observed on the parts of a sculpture that have been washed away by rain. In addition, if the aqueous film is highly acidic ($\text{pH} < 3.5$), brochantite dissolves, and antlerite may precipitate [12,13,42–48]. It is in line with the finding that cuprite in the copper patina that is exposed to an outdoor environment for a long time (7–300 years) continues to grow for up to 15 years, following which, the corrosion rate is consistently maintained while brochantite grows annually by $0.15 \mu\text{m}$ [23].

5. Conclusions

A corrosion experiment on artificial sulfide patina was conducted to investigate the corrosion characteristics of the outdoor bronze sculptures found in an urban–industrial environment, and the results are as follows.

The correlation between the chromaticity and reflectance of the patina and corrosion products showed that the amount of brochantite increased with the corrosion of sulfide patina and that chromaticity a^* was associated with patina growth. Furthermore, cuprite and brochantite were distinguished, and the point at which green brochantite began to cover the patina surface was determined. In particular, 20% reflectance in the yellow–red wavelength (565–750 nm) region was the inflection point for identifying cuprite and brochantite.

The correlation between the composition and corrosion products of the patina revealed that the major factors determining the quantitative changes in brochantite include physical causes such as crystal size and patina layer thickness; another factor is the increase in Cu that occurs when Cu^{2+} ions working as color formation ions move to the outermost layer.

The atmospheric corrosion of the Cu–Zn–Sn–Pb quaternary bronze confirmed through the corrosion experiment on the artificial patina resulted in reduced contents of the base metals Cu and Zn but increased contents of Sn and Pb. The decreased Cu and Zn contents are respectively attributable to the selective dissolution of Cu and Zn ions owing to decuprification and dezincification within bronze, in which the cation moves toward the boundary through the patina inside the alloy, while Sn forms a patina layer by being condensed as insoluble corrosion products for a stabilization effect. To date, the atmospheric corrosion of bronze has been considered to exhibit reactions similar to those of pure copper; however, the corrosion process of bronze differs depending on the alloying elements.

The microstructure of the sulfide patina was confirmed to consist of brochantite in the outermost layer and cuprite and cassiterite in the inner layers. The cuprite layer was generated early in the corrosion experiment and remained uniform, and cassiterite was formed around the pitting between the base metal and cuprite. The patina structure was distinguished into cuprite, cassiterite, and a mixed layer of cuprite–cassiterite based on the Cu/Sn contents as well as structure layer and color. Brochantite in the outer layer grew continuously into a flower-shaped aggregate formed by needle-like crystals.

This study examined the characteristics of sulfide patina according to the corrosion behavior, and its findings are expected to be utilized in future studies on the corrosion characteristics of outdoor bronze sculptures.

Author Contributions: Conceptualization, N.C.; Methodology, H.K.; Software, H.K.; Validation, H.K.; Formal Analysis, H.K.; Investigation, H.K.; Resources, N.C.; Data Curation, H.K.; Writing—Original Draft Preparation, H.K.; Writing—Review and Editing, N.C.; Visualization, H.K.; Supervision, N.C.; Project Administration, N.C.; Funding Acquisition, H.K. All authors have read and agreed to the published version of the manuscript.

Funding: This research was funded by the Conservation Science Research Project of the National Museum of Modern and Contemporary Art, Republic of Korea (MMCA).

Data Availability Statement: Not applicable.

Conflicts of Interest: The authors declare no conflict of interest. The sponsors had no role in the design, execution, interpretation, or writing of the study.

References

1. Buccolieri, G.; Castellano, A.; Serra, A.; Zavarise, G.; Palmiero, E.; Buccolieri, A. Archaeometric analysis of patinas of the out-door copper statue Sant'Oronzo (Lecce, Italy) preparatory to the restoration. *Microchem. J.* **2020**, *154*, 104538. [[CrossRef](#)]
2. Buccolieri, G.; Buccolieri, A.; Donati, P.; Marabelli, M.; Castellano, A. Portable EDXRF investigation of the patinas on the Riace Bronzes. *Nucl. Instrum. Methods Phys. Res. B* **2015**, *343*, 101–109. [[CrossRef](#)]
3. Young, M.L.; Schnepf, S.; Casadio, F.; Lins, A.; Meighan, M.; Lambert, J.B.; Dunand, D.C. Matisse to Picasso: A compositional study of modern bronze sculptures. *Anal. Bioanal. Chem.* **2009**, *395*, 171–184. [[CrossRef](#)] [[PubMed](#)]
4. Day, J.; Stenger, J.; Eremin, K.; Khandekar, N.; Budny, V. Gaston Lachaise's bronze sculpture in the Fogg Museum. *J. Am. Inst. Conserv.* **2010**, *49*, 1–26. [[CrossRef](#)]
5. Ganio, M.; Leonard, A.; Plisson, J.S.; Walton, M. From sculptures to foundries: Elemental analysis to determine the provenance of modern bronzes. In Proceedings of the 15ème journées d'étude de la SFIIC-ICOMOS, Paris, France, 4–5 December 2014; pp. 136–144.
6. Young, M.L.; Dunand, D.C. Comparing compositions of modern cast bronze sculptures: Optical emission spectroscopy versus X-ray fluorescence spectroscopy. *Miner. Met. Mater. Soc.* **2015**, *67*, 1646–1658. [[CrossRef](#)]
7. Randall, M.; Zycherman, L.; Griffith, R. Conservation of Joan Miró's bronze sculptures at the Museum of Modern Art. *AIC Objects Spec. Group Postprints* **2016**, *23*, 233–255.
8. Pouyet, E.; Ganio, M.; Motlani, A.; Saboo, A.; Casadio, F.; Walton, M. Casting light on 20th-century Parisian artistic bronze: Insights from compositional studies of sculptures using hand-held X-ray fluorescence spectroscopy. *Heritage* **2019**, *2*, 732–748. [[CrossRef](#)]
9. Kwon, H.H. The Corrosion Characteristics and Applicability of Non-Destructive Investigation in the Outdoor Bronze Sculptures. Ph.D. Thesis, Kongju National University, Gongju, Republic of Korea, 2023; pp. 6–43.
10. Yonehara, M.; Matsui, T.; Kihara, K.; Isono, H.; Kijima, A.; Sugibayashi, T. Experimental relationships between surface roughness, glossiness and color of chromatic colored metals. *Mater. Trans.* **2004**, *45*, 1027–1032. [[CrossRef](#)]
11. Radivojević, M.; Pendić, J.; Srejić, A.; Korać, M.; Davey, C.; Benzonelli, A.; Martínón-Torres, M.; Jovanović, N.; Kamberović, Z. Experimental design of the Cu-As-Sn ternary colour diagram. *J. Archaeol. Sci.* **2018**, *90*, 106–119. [[CrossRef](#)]
12. Strandberg, H. Reactions of copper patina compounds—I. Influence of some air pollutants. *Atmos. Environ.* **1998**, *32*, 3511–3520. [[CrossRef](#)]
13. Krätschmer, A.; Wallinder, I.O.; Leygraf, C. The evolution of outdoor copper patina. *Corros. Sci.* **2002**, *44*, 425–449. [[CrossRef](#)]
14. Bongiorno, V.; Campodonico, S.; Caffara, R.; Piccardo, P.; Carnasciali, M.M. Micro-Raman spectroscopy for the characterization of artistic patinas produced on copper-based alloys. *J. Raman Spectrosc.* **2012**, *43*, 1617–1622. [[CrossRef](#)]
15. Carlo, G.D.; Giuliani, C.; Riccucci, C.; Pascucci, M.; Messina, E.; Fierro, G.; Lavorgna, M.; Ingo, G.M. Artificial patina formation onto copper-based alloys: Chloride and sulphate induced corrosion processes. *Appl. Surf. Sci.* **2017**, *421*, 120–127. [[CrossRef](#)]
16. Bureš, R.; Rak, P.; Stoužil, J. Long-term outdoor exposure of artificial copper patina based on brochantite. *Koroze Ochr. Mater.* **2020**, *64*, 87–94. [[CrossRef](#)]
17. Moon, D.H.; Han, M.S.; Jeong, H.Y.; Go, I.H.; Cho, H.G. Mineral compositions of Korean Dancheong pigment products using quantitative XRD. *J. Conserv. Sci.* **2016**, *32*, 403–415. [[CrossRef](#)]
18. Strandberg, H. Perspectives on Sculpture Conservation: Modelling Copper and Bronze Corrosion. Ph.D. Thesis, University of Gothenburg, Gothenburg, Sweden, 1997; pp. 7–107.
19. Kwon, H.H.; Kim, Y.S.; Kim, B.J.; Choi, N.Y.; Park, H.S.; Kim, J.S. A study on conservation and material characteristics of out-door bronze sculpture: Kim Chan Shik's 'Feeling'. *J. Conserv. Sci.* **2017**, *33*, 155–165. [[CrossRef](#)]
20. Masi, G.; Esvan, J.; Josse, C.; Chiavari, C.; Bernardi, E.; Martini, C.; Bignozzi, M.C.; Gartner, N.; Kosec, T.; Robbiola, L. Characterization of typical patinas simulating bronze corrosion in outdoor conditions. *Mater. Chem. Phys.* **2017**, *200*, 308–321. [[CrossRef](#)]
21. Masi, G.; Bernardi, E.; Martini, C.; Vassura, I.; Skrlep, L.; Fabjan, E.S.; Gartner, N.; Kosec, T.; Josse, C.; Esvan, J.; et al. An innovative multi-component fluoropolymer-based coating on outdoor patinated bronze for Cultural Heritage: Durability and reversibility. *J. Cult. Herit.* **2020**, *45*, 122–134. [[CrossRef](#)]
22. Scott, D.A. *Metallography and Microstructure of Ancient and Historic Metals*; The Getty Conservation Institute: Los Angeles, CA, USA, 1991; pp. 2–10.
23. FitzGerald, K.P.; Nairn, J.; Skennerton, G.; Atrons, A. Atmospheric corrosion of copper and the colour, structure and composition of natural patinas on copper. *Corros. Sci.* **2006**, *48*, 2480–2509. [[CrossRef](#)]
24. Graedel, T.E.; Nassau, K.; Franey, J.P. Copper patinas formed in the atmosphere—I. Introduction. *Corros. Sci.* **1987**, *27*, 639–657. [[CrossRef](#)]
25. Franey, J.P.; Davis, M.E. Metallographic studies of the copper patina formed in the atmosphere. *Corros. Sci.* **1987**, *27*, 659–668. [[CrossRef](#)]
26. Ropret, P.; Kosec, T. Raman investigation of artificial patinas on recent bronze—Part I: Climatic chamber exposure. *J. Raman Spectrosc.* **2012**, *43*, 1578–1586. [[CrossRef](#)]
27. Kosec, T.; Ropret, P.; Legat, A. Raman investigation of artificial patinas on recent bronze—Part II: Urban rain exposure. *J. Raman Spectrosc.* **2012**, *43*, 1587–1595. [[CrossRef](#)]
28. Catelli, E.; Sciutto, G.; Prati, S.; Jia, Y.; Mazzeo, R. Characterization of outdoor bronze monument patinas: The potentialities of near-infrared spectroscopic analysis. *Environ. Sci. Pollut. Res.* **2018**, *25*, 24379–24393. [[CrossRef](#)]
29. Crippa, M.; Bongiorno, V.; Piccardo, P.; Carnasciali, M.M. A characterisation study on modern bronze sculpture: The artistic patinas of Nado Canuti. *Stud. Conserv.* **2019**, *64*, 16–23. [[CrossRef](#)]

30. Piccardo, P.; Mille, B.; Robbiola, L. Tin and copper oxides in corroded archaeological bronzes. In *Corrosion of Metallic Heritage Artefacts*; Woodhead Publishing: Sawston, UK, 2007; pp. 239–262.
31. Bernardi, E.; Chiavari, C.; Lenza, B.; Martini, C.; Morselli, L.; Ospitali, F.; Robbiola, L. The atmospheric corrosion of quaternary bronzes: The leaching action of acid rain. *Corros. Sci.* **2009**, *51*, 162–169. [[CrossRef](#)]
32. Oudbashi, O. Multianalytical study of corrosion layers in some archaeological copper alloy artefacts. *Surf. Interface Anal.* **2015**, *47*, 1138–1146. [[CrossRef](#)]
33. Sebar, L.E.; Iannucci, L.; Gori, C.; Re, A.; Parvis, M.; Angelini, E.; Grassini, S. In-situ multi-analytical study of ongoing corrosion processes on bronze artworks exposed outdoors. *ACTA IMEKO* **2021**, *10*, 241–249. [[CrossRef](#)]
34. Basso, E.; Pozzi, F.; Reiley, M.C. The *Samuel, F.B. Morse* statue in Central Park: Scientific study and laser cleaning of a 19th century American outdoor bronze monument. *Herit. Sci.* **2020**, *8*, 7–12. [[CrossRef](#)]
35. Catelli, E.; Randeberg, L.L.; Strandberg, H.; Alsberg, B.K.; Maris, A.; Vikki, L. Can hyperspectral imaging be used to map corrosion products on outdoor bronze sculptures? *J. Spectr. Imaging* **2018**, *7*, a10. [[CrossRef](#)]
36. Leygraf, C.; Chang, T.; Herting, G.; Wallinder, I.O. The origin and evolution of copper patina colour. *Corros. Sci.* **2019**, *157*, 337–346. [[CrossRef](#)]
37. Chiavari, C.; Rahmouni, K.; Takenouti, H.; Joiret, S.; Vermaut, P.; Robbiola, L. Composition and electrochemical properties of natural patinas of outdoor bronze monuments. *Electrochim. Acta* **2007**, *52*, 7760–7769. [[CrossRef](#)]
38. Robbiola, L.; Rahmouni, K.; Chiavari, C.; Martini, C.; Prandstraller, D.; Texier, A.; Takenouti, H.; Vermaut, P. New insight into the nature and properties of pale green surfaces of outdoor bronze monuments. *Appl. Phys. A* **2008**, *92*, 161–169. [[CrossRef](#)]
39. Papadopoulou, O.; Delagrammatikas, M.; Vassiliou, P.; Grassini, S.; Angelini, E.; Gouda, V. Surface and interface investigation of electrochemically induced corrosion on a quaternary bronze. *Surf. Interface Anal.* **2014**, *46*, 771–775. [[CrossRef](#)]
40. Fitzgerald, K.P.; Nairn, J.; Atrens, A. Surface characterization of artificial corrosion layers on copper alloy reference materials. *Appl. Surf. Sci.* **2002**, *189*, 90–101.
41. Chiavari, C.; Bernardi, E.; Martini, C.; Passarini, F.; Ospitali, F.; Robbiola, L. The atmospheric corrosion of quaternary bronzes: The action of stagnant rain water. *Corros. Sci.* **2010**, *52*, 3002–3010. [[CrossRef](#)]
42. Robbiola, L.; Hurltel, L.P. New contribution to the study of corrosion mechanisms of outdoor bronzes: Characterization of the corroding surfaces of Rodin's bronzes. *Mem. Etudes Sci. Rev. Metall.* **1991**, *88*, 809–823.
43. Robbiola, L.; Fiaud, C.; Pennec, S. New model of outdoor bronze corrosion and its implications for conservation. In *ICOM Committee for Conservation 10th Triennial Meeting*; HAL Open Science: Lyon, France, 1993; pp. 796–801.
44. Strandberg, H.; Johansson, G.; Rosvall, J. Outdoor bronze sculptures—A conservation view on the examination of the state of preservation. In *Proceedings of the ICOM Committee for Conservation 11th Triennial Meeting*, Edinburgh, Scotland, 1–6 September 1996; pp. 894–900.
45. Selwyn, L.S.; Binnie, N.E.; Poitras, J.; Laver, M.E.; Downham, D.A. Outdoor bronze statues: Analysis of metal and surface samples. *Stud. Conserv.* **1996**, *41*, 205–228.
46. Scott, D.A. *Copper and Bronze in Art: Corrosion, Colorants and Conservation*; Getty Publication: Los Angeles, CA, USA, 2002; pp. 43–59, 81–99, 122–167.
47. Fuente, D.; Simancas, J.; Morcillo, M. Morphological study of 16-year patinas formed on copper in a wide range of atmospheric exposures. *Corros. Sci.* **2008**, *50*, 268–285. [[CrossRef](#)]
48. Gianni, L. Corrosion Behavior of Bronze Alloys Exposed to Urban and Marine Environment: An Innovative Approach to Corrosion Process Understanding and to Graphical Results Presentation. Ph.D. Thesis, University of Ghent, Ghent, Belgium, 2011; pp. 7–27.

Disclaimer/Publisher's Note: The statements, opinions and data contained in all publications are solely those of the individual author(s) and contributor(s) and not of MDPI and/or the editor(s). MDPI and/or the editor(s) disclaim responsibility for any injury to people or property resulting from any ideas, methods, instructions or products referred to in the content.